ACS OMEGA

Open Access

http://pubs.acs.org/journal/acsodf

Article

Dual Functional Nanostructured Nickel Electrodes on Anodic Alumina for Energy Storage Applications

Tabish Aftab, Josep Ferre-Borrull,* and Lluis F. Marsal

Cite This: *ACS Omega* 2025, 10, 24618−24627

Read Online

ACCESS | Metrics & More | Article Recommendations | Supporting Information

ABSTRACT: This study presents a novel approach for fabricating nickel-based nanorod electrodes with dual electrochemical functionality, bridging supercapacitive and faradaic applications. Using nanoporous anodic alumina (NAA) templates and a pulsed electrodeposition technique, two distinct electrode configurations were engineered from a single presubstrate: nickel nanorods in NAA with partially dissolved pore walls (Ni-NR@NAA) and free-standing nickel nanorods after NAA removal and Ni redeposition (Ni-R-NR@NAA). Structural analysis via field-emission scanning electron microscopy (FESEM) confirmed the uniformity and integrity of the nanorods, while their electrochemical performance was evaluated by cyclic voltammetry (CV). The Ni-NR@NAA electrodes demonstrated the pseudocapacitive performance, achieving a capacitance per unit area of 104 $mFcm^{-2}$, which is nearly seven times higher than flat nickel electrodes, attributed to the enhanced active surface area and efficient ion transport. Specific capacitance can reach up to 60 Fg^{-1} at low scan rates. In contrast, the Ni-R-NR@NAA electrodes exhibited predominantly capacitive behavior with reduced redox activity due to structural modifications. These results emphasize the critical role of nanostructural design in tuning the electrochemical performance, offering a versatile platform for advanced energy storage devices capable of dual supercapacitive and faradaic functionality.

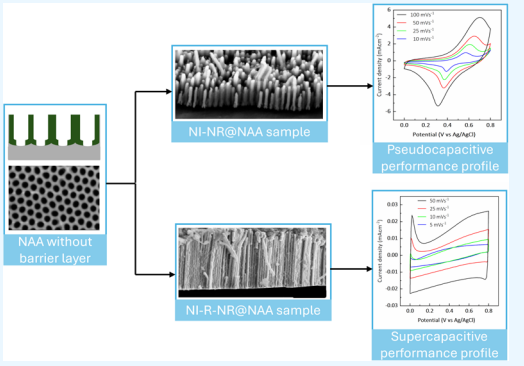

INTRODUCTION

In the rapidly evolving era of energy storage technologies, the development of high-performance supercapacitors and pseudocapacitors has attracted considerable attention. These devices, renowned for their high charge storage capacities, rapid charge−discharge speeds, and remarkable durability over several cycles, play a vital role in the advancement of portable electronics, electric cars, and grid energy storage solutions.[1−4] Supercapacitors (SCs), known for their distinctive power density, store electrical charge through the formation of an electric double layer, while pseudocapacitors (PSCs) employ faradaic redox reactions to achieve a higher energy density. The fast charge−discharge kinetics are characteristic of supercapacitors, whereas the energy-rich redox processes are a defining feature of pseudocapacitors. To meet the rising energy demands of high-performance energy systems, particularly for motor vehicles and portable electronic devices, SCs and PSCs are emerging as a highly promising option, positioning them as a leading candidate for next-generation high-energy storage solutions.[5,6] The electrode material plays a crucial role in determining the overall efficiency and effectiveness of the energy storage systems.[7,8] Nanostructured materials are crucial for developing electrodes with remarkable electrochemical properties due to their high surface area, short ion diffusion paths, and superior conductivity. These features enhance capacity, charge/discharge rates, and durability, making them ideal for advanced energy storage systems.[9−12]

Nanostructures composed of nickel have garnered significant interest because of their exceptional electrical conductivity, strong electrochemical activity, and intrinsic chemical stability. Different nanostructured nickel electrodes such as nickel nanowires,[13] nickel nanoflakes,[14] nickel nanospheres,[15] and nickel nanoporous structures[16] utilized as electrode materials for energy devices have already been studied. Nevertheless, the challenge of optimizing these nanostructures to achieve improved performance in energy storage applications continues.[17−20]

Nanoporous anodic alumina (NAA) is a highly ordered nanochannel membrane obtained by the anodization of pure aluminum.[21−23] It consists of longitudinal pores perpendicular to the material surface where the pore length, interpore distance, and pore diameter can be tuned in a broad range of possible values. NAA can be used as a template to achieve nanostructuring of different materials such as polymers[24,25] or metals[26−28] with adjustable geometries. The NAA template technique has been commonly employed to obtain nano-

Received: February 13, 2025
Revised: May 8, 2025
Accepted: May 14, 2025
Published: June 6, 2025

structured nickel, cobalt, and nickel−cobalt nanostructures for applications in hydrogen production or sensing.[29,30] The same technique has also been applied to obtain nanostructured electrodes for energy storage application; for instance, Han et al.[31] obtained nanostructured dielectric capacitors by infiltrating carbon nanotubes in two different types of NAA pores: Xu et al.[32,33] demonstrated the preparation of cobalt oxide and nickel oxide nanotubes in NAA with supercapacitive properties and Nakanishi et al.[34] electrochemically deposited gold in the NAA pores to obtain nanowires with fast ion and electron transport properties.

Similarly, González et al. reported the development of NAA nanostructured patterned Ag electrodes for supercapacitor applications. Their approach involved fabricating an initial Ag antidot thin film via thermal vacuum deposition followed by electroplating using a commercial Ag electrolyte to obtain a conformal silver nanolayer. This nanostructured Ag film served as the final active electrode, demonstrating the versatility of NAA templates in developing high-performance metallic electrodes.[35]

Therefore, in this work, we utilize the NAA templating technique to obtain nickel nanorod array structures with contact on the aluminum substrate with the aim of studying their electrochemical properties in relation to supercapacitor and pseudocapacitor applications.

We obtained nickel nanorod structures by electrochemical deposition within the pore walls. This is achieved by removing the barrier layer at the bottom of the pores and enabling contact of the electrolyte with the aluminum substrate. With this, the electrochemical deposition results in metallic nickel filling the pores in contact with the aluminum substrate, which can be used as a conductive interface with the external circuit. However, to enable electrochemical reactions to take place, it is necessary to remove the alumina pore walls so that electrolyte ions can diffuse to the nickel nanorods surface, while at the same time preventing the electrolyte from reaching the aluminum substrate and causing unwanted reactions. We followed two routes to this end: (i) a partial dissolution of the alumina pore walls and (ii) a complete dissolution of the alumina and a subsequent deposition of nickel that covers the aluminum. In the first case, the partial dissolution of alumina leaves a layer of oxide that separates the substrate aluminum from the electrolyte. In the second case, the further deposited nickel covers the aluminum, avoiding any contact of the substrate with the electrolyte ions.

In the following, two different routes to obtain nanostructured electrodes are described as well as their structural characterization performed using field-emission scanning electron microscopy (FESEM) and their electrochemical behavior evaluated through cyclic voltammetry (CV). The results are thoroughly analyzed and discussed, and the conclusions are drawn.

MATERIAL AND METHODS

Materials Used. Aluminum sheets with 99.999% purity and a thickness of 0.5 mm were purchased from Goodfellow, U.K. The reagents for anodization, such as oxalic acid ($C_2H_2O_4{\cdot}2H_2O$), phosphoric acid (H_3PO_4), and chromic acid (H_2CrO_4), were obtained from Sigma-Aldrich, U.K. For pulsed electrodeposition, chemicals including nickel sulfate ($NiSO_4{\cdot}6H_2O$), nickel chloride ($NiCl_2{\cdot}6H_2O$), boric acid (H_3BO_3), and potassium hydroxide (KOH) were also bought from Sigma-Aldrich, U.K. Deionized water with a resistivity of 18.2 MΩ·cm, prepared using an Elga Purelab Chorus system from Elga Labwater Corp., U.K., was used throughout all our experiments.

Characterization Techniques Used. *Structural Characterization.* The structural morphology of the fabricated samples was analyzed using a field-emission scanning electron microscopy (FESEM, model Scios 2 by FEI Company, Hillsboro, OR) instrument operated at an accelerating voltage of 20 kV. The samples were utilized in their natural, untreated state due to their inherent conductivity. The micrographs obtained provided detailed insights into the surface morphology and structural integrity of the nickel nanostructured electrodes.

Electrochemical Characterization. Electrochemical measurements were conducted by using cyclic voltammetry (CV) to assess the electrochemical properties of both types of nickel nanostructured samples. Experiments were performed with a potentiostat (model sModule 2.5 A/10 V from Ivium Technologies BV, Eindhoven, The Netherlands) in a three-electrode cell setup. The reference electrode used was an Ag/AgCl electrode (RE 1CP type, obtained from ALS, Tokyo, Japan), while a platinum spiral wire served as the counter electrode and the nickel nanostructured samples acted as the working electrode. The area of the Ni nanorod samples exposed to the electrolyte was 0.7 cm^2. CV scans were executed over a potential range from 0 to 0.8 V, employing different scan rates ranging from 5 to 100 mVs^{-1} in 1 M KOH solution. The resulting CV curves provided insights into the redox processes and capacitance behaviors of our samples. Data analysis was performed by using IviumSoft software.

Capacitance was calculated from the CV using the formula based on the area enclosed in the CV curve and detailed in Supporting Information, eq (1). Specific capacitance was obtained considering the mass of deposited nickel in the samples and calculated as specified in Supporting Information, eq (2).

Fabrication of Nanoporous Anodic Alumina. The fabrication of nanoporous anodic alumina (NAA) was performed using the established two-step anodization method outlined by Masuda et al.[22] High-purity aluminum sheets were precisely cut into 2 cm × 2 cm pieces, ensuring no bending occurred. These pieces were mechanically cleaned via ultrasonication in water and acetone to remove impurities, followed by thorough drying. The pieces were then mounted in a custom-designed PVC casing (shown in Figure S1) used throughout the electrochemical procedures. In this experimental setup, the aluminum pieces constitute the anode and are mounted on a copper plate connected to the source, while a platinum wire serves as the cathode.[36]

To minimize surface roughness of aluminum on the electrolyte side, electrochemical polishing was performed prior to anodization in the same cell with a perchloric acid and water mixture (1:4 ratio) at 2 °C for 5 min. This process involved applying a 20 V DC voltage using a current source (model SM300-5 from Delta Elektronika, Zierikzee, The Netherlands) connected with two digital multimeters (model 34401A from Agilent, Santa Clara, CA) to measure and transfer the current and voltage data to a computer. After electropolishing, the samples were rinsed with water and ethanol and dried with compressed air, making them ready for the first anodization step.

NAA templates were synthesized using a 0.3 M oxalic acid solution as the electrolyte.[37] The first anodization was carried

https://doi.org/10.1021/acsomega.5c01368
ACS Omega 2025, 10, 24618−24627

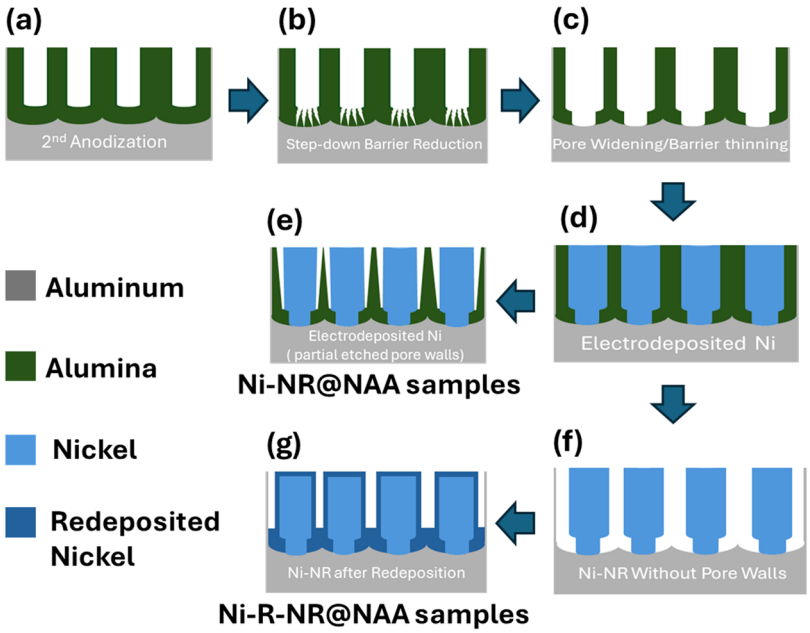

Figure 1. Scheme of the process to produce nickel nanorod arrays on aluminum substrates. (a) Nanoporous anodic alumina after the two-step anodization process. (b) Structure after the anodization current step-by-step reduction. (c) Structure after the residual oxide thickness dissolution. It can be observed as there is a contact of the substrate aluminum with the pores' inner volume. (d) NAA after the pulsed electrodeposition of nickel in the pores. (e) Ni-NR@NAA structure after the partial dissolution of NAA pore walls. The nickel nanorods maintain electrical contact with the aluminum substrate. There is a space around the nanorods for electrochemical interaction and there is an oxide layer that isolates the substrate aluminum from the inner pore volume. (f) NAA with the nickel nanorods after the complete dissolution of NAA pore walls. (g) Ni-R-NR@NAA after redeposition of nickel. The nanorods have electrical contact with the substrate aluminum, while there is no direct contact of this aluminum with the inner pore volume.

out at 40 V using a source-meter (model Keithley-2420 from Tektronix, Beaverton, OR) at 5 °C for 20 h, resulting in a layer of NAA with randomly arranged pores at the top of the oxide layer that become self-arranged at the oxide−aluminum interface. The resulting Al_2O_3 layer was then removed by immersing the samples in a solution of chromic and phosphoric acids (1.8 and 6 wt %, respectively) at 70 °C for 3 h. When the pores were completely dissolved, the samples were rinsed with ethanol and water. This leaves an aluminum surface with texturized concavities arranged in a quasi-periodic lattice that act as nucleation points for the ordered pore growth in the second anodization.[38]

After complete drying, a second anodization was carried out under the same conditions (40 V, 5 °C) for 2 h to achieve the desired nanopore length of approximately 2 μm. This process yields an NAA layer with self-organized pores in a quasi-hexagonal pattern with a uniform pore diameter and interpore distance.

In Situ Barrier Layer Removal. The resulting NAA obtained after the second anodization (Figure 1a) possesses a barrier oxide layer at the base of its pores, with a thickness ranging from approximately 40 to 50 nm. It is essential to remove this barrier layer in order to enable electrical contact between the aluminum substrate and the inner pore channels. This removal was achieved using the step-down voltage reduction technique as outlined by Santos et al.[39] This method involves a gradual step-by-step reduction of the anodization current, performed in the same electrochemical cell setup and utilizing the same 0.3 M oxalic acid electrolyte as used in the second anodization process. This is why the technique is also termed the third anodization or in situ barrier layer removal method. At each step, the current is instantaneously reduced by a constant factor, causing the anodization potential between the samples to gradually decrease until it stabilizes. At this point, the next step of the current reduction is initiated. This sequence continues until the potential reaches between 6 and 7 V. Given the direct relationship between potential and barrier layer thickness, this results in a barrier layer with nanochannels that reach almost to the aluminum substrate and a residual oxide thickness of less than 10 nm (Figure 1b). Further reduction of the potential could lead to the complete detachment of the oxide structure from the aluminum substrate. To remove the residual oxide thickness, the sample was immersed in a 5 wt % H_3PO_4 solution at 35 °C for 15 min. This step effectively dissolves the residual oxide thickness while simultaneously enlarging the pore diameter (Figure 1c). Microscopy images of NAA samples with and without the barrier layer are shown in Figure S2.

Pulsed Electrodeposition of Nickel. For the pulsed electrodeposition (PED) of nickel, the obtained NAA was set up as a working electrode in an electrochemical cell, whereas platinum served as the counter electrode. The electrolyte used is commonly known as Watts bath and consists of 300 g of nickel sulfate, 45 g of nickel chloride, and 45 g of boric acid (used as buffer) diluted in deionized 1 l of water with pH maintained at 4.5 by adding KOH.[26] The electrolyte was kept at constant room temperature during the deposition procedure. In this process, as described by Nielsch et al.,[40] instead of applying a constant electric current, the current is applied in periodic intervals consisting of consecutive pulses (short bursts) of negative, positive, and zero intensity. When the current is negative, the sample acts as the cathode, and nickel ions from the solution are reduced and electrodeposited on the metal−electrolyte interface at the bottom of

https://doi.org/10.1021/acsomega.5c01368
ACS Omega 2025, 10, 24618−24627

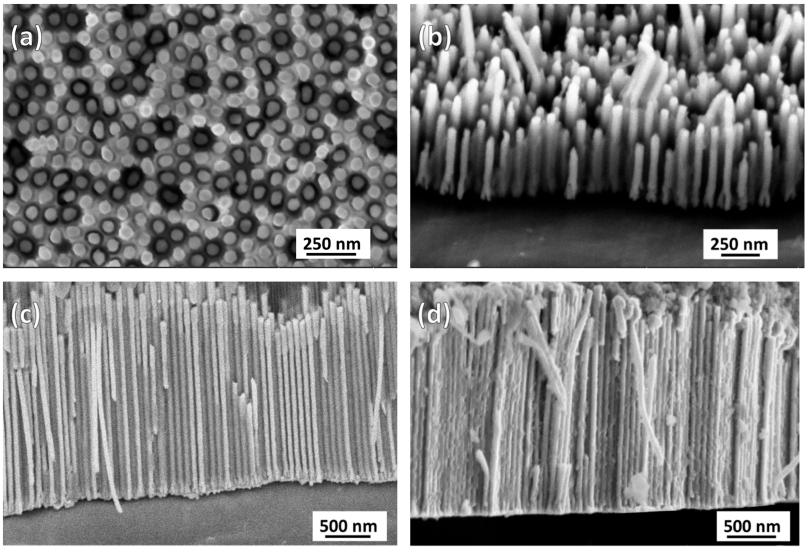

Figure 2. FESEM images of (a, b) top and cross-sectional views of samples with partially etched pore wall nickel nanorod samples (Ni-NR@NAA), respectively, and (c, d) cross-sectional views before and after redeposition on completely etched pore wall nickel nanorod samples, respectively.

the pores, forming nickel nanorods. Since the volume within the pores is very small, this causes a depletion of nickel ions after a short time. For this reason, the polarity of the current is changed, permitting a recovery of the nickel ion concentration close to the metal−electrolyte interface by favoring ion diffusion. By repeating these cycles, nickel gradually builds up inside the alumina pores layer by layer resulting in a uniform nickel filling in the form of nanorods inside the pores of alumina (Figure 1d). The cycles are repeated until a predefined charge is employed, Q_{dep}, defined as the integral over time of the applied current. This deposition charge was controlled to ensure the filling of the pores up to a desired level and avoid overflow. Figure S3 shows the cross section and the top view of alumina pores filled with nickel.

Nickel Nanorod Samples (Ni-NR@NAA) Preparation. The nickel-deposited NAA was immersed in a 5 wt % phosphoric acid solution at 35 °C for a short duration of 5 min. This process was designed to partially dissolve the alumina pore walls. Thinning the pore walls allows the electrolyte to infiltrate the space between the nickel and the alumina while maintaining the mechanical integrity of the nickel nanorods and ensuring their electrical contact with the aluminum substrate. At the same time, the partial dissolution of the oxide leaves a residual oxide thickness at the pore base that isolates the aluminum substrate of direct contact with the electrolyte (Figure 1e).

Nickel Redeposited Nanorod Samples (Ni-R-NR@NAA) Preparation. To prepare these samples, we started with the same procedure as outlined for the Ni-NR@NAA: the nickel-deposited NAA (Figure 1d) was immersed in a 5 wt % phosphoric acid solution at 35 °C, but in this case, for an extended period of 12−15 min to fully dissolve the alumina pore walls. This results in free-standing nickel nanorods with contact with the aluminum substrate (Figure 1f). Subsequently, nickel deposition was repeated using the same pulsed electrodeposition technique previously described for a total employed charge Q_{redep}. This step was carried out to ensure that the aluminum surface exposed to the electrolyte after fully dissolving the oxide is completely covered with nickel (Figure 1g), preventing any reactivity of aluminum with the electrolyte during electrochemical characterization.

RESULTS AND DISCUSSION

The samples at different stages of preparation were examined by means of field-emission scanning electron microscopy (FESEM). Nanoporous anodic alumina (NAA) layers on the aluminum substrate with well-organized and uniformly distributed pores were obtained by the described two-step anodization process (SEM image shown in Figure S2). After the removal of the barrier layer and further etching (to eliminate the residual barrier layer and form the electrical pathway between the pore interior and the substrate aluminum), the pore diameter, interpore spacing, and pore wall thickness were estimated to be 60−70, 90−100, and 20−30 nm, respectively.

After nickel pulsed electrodeposition, the obtained samples are illustrated in Figure S3. The cross section in Figure S3a indicates that Ni fills the pores and keeps contact with the aluminum substrate, which provides integrity and mechanical strength to the standing Ni nanorods. The top view image (Figure S3b) shows that the level of filling is not uniform, as indicated by the different gray tones of different pores. Figure S3c depicts in detail the shape of the nickel nanorods at their contact with the substrate. Such a shape is a result of the barrier layer thinning procedure: the thinning is not uniform but consists of the formation of nanochannels from the bottom of the pores to the aluminum. When these nanochannels are filled with electrodeposited Ni, they form paw-like structures at the base of the nanorods.

After the acquisition of the two different kinds of samples, Ni-NR@NAA and Ni-R-NR@NAA, their morphology was also examined with FESEM. Figure 2 shows representative images of the obtained results. Figure 2a shows the top view of a Ni-NR@NAA, while Figure 2b shows a corresponding cross section. On the other hand, Figure 2c shows a Ni-R-NR@NAA sample after the complete removal of the alumina and before the redeposition process, while Figure 2d shows a sample obtained with the same Q_{dep} after the redeposition step.

https://doi.org/10.1021/acsomega.5c01368
ACS Omega 2025, 10, 24618−24627

The top view picture of the Ni-NR@NAA sample shows the alumina structure with a nickel nanorod inside each of the pores. It can be observed that the nanorods are surrounded by a ring with darker tone, confirming that a space between the rods and the alumina pore walls has been created. The cross section in Figure 2b shows the nanorods with variable rod length and in contact with the substrate aluminum. The remaining pore walls can be seen as a lighter gray shade between the rods, which appear in a brighter tone.

The cross section for the Ni-R-NR@NAA sample (Figure 2c) shows a structure with longer rods as in parts a and b and without the alumina surrounding the nanorods. For this specific sample, the diameter of nanorods was approximately 65−70 nm, while the average length was estimated to be 2 μm. After the redeposition, the rods appear to be thicker and show a bigger roughness and even the attachment of some spherical nickel aggregates. Also, a compact nickel layer can be observed at the bottom of the nanorods where they contact the aluminum. This compact nickel layer is not present in Figure 2c and will prevent reaction of the electrolyte with the substrate aluminum during CV measurements.

Figure 3 shows a comparison between the characteristic cyclic voltammetry (CV) curves of a pure (flat) Ni surface and

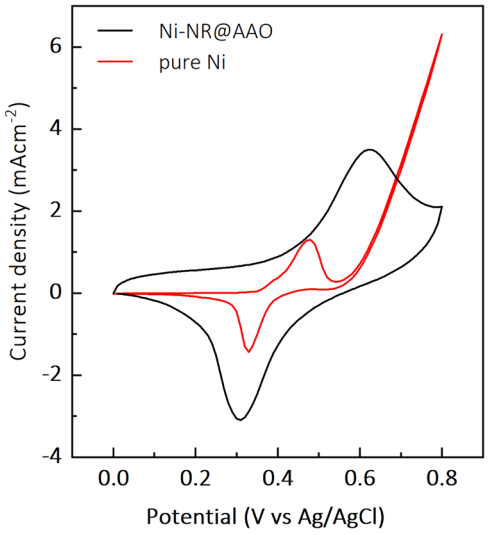

Figure 3. CV curve of Ni-NR@NAA nanorods and pure nickel, as the working electrode with reference to Ag/AgCl in 1 M KOH solution electrolyte.

a Ni-NR@NAA obtained with Q_{dep} = 3.5 C. This charge corresponds to a mass loading of nickel of 574 μg. The calculation of this mass loading is explained in the Supporting Information. The current density (j) versus potential (E) measurements were taken under the same conditions for both samples at a scan rate of 50 mVs^{-1} and after 500 cycles. Both CV curves exhibit characteristic oxidation and reduction peaks, indicating an evident faradaic behavior.

The oxidation (anodic) peak for the pure Ni reaches at j_{pa} = 1.13 mA·cm^{-2}, while for the reduction (cathodic) peak it decreases to j_{pc} = −1.44 mA·cm^{-2}. On the other hand, the oxidation and reduction peaks for Ni-NR@NAA reach j_{pa} = 3.50 mA·cm^{-2} and j_{pc} = −3.09 mA·cm^{-2}, respectively. The oxidation and reduction peaks appear at E_{pa} = 0.45 V and E_{pc} = 0.33 V, respectively, for the flat Ni, while the peaks shift to E_{pa} = 0.60 V and E_{pc} = 0.31 V for Ni-NR@NAA.

The capacitance per unit area, C', can be estimated from the CV curves using the capacitance formula outlined in ref 41 and taking into account the area of the sample exposed to the electrolyte. Details of such calculation are given in the Supporting Information. With this, C' = 15 mF·cm^{-2} for the flat Ni and C' = 104 mF·cm^{-2} for Ni-NR@NAA, which indicates close to a 7-fold increase with the nanostructuring. Additionally, the onset of the oxygen evolution reaction (OER) is observed at approximately 0.6 V in flat Ni, but it is not found in the case of Ni-NR@NAA.

Finally, the beginning of the anodic part of the CV curve for Ni-NR@NAA (at 0 V) shows a fast increase of Δj = 0.45 mA·cm^{-2} in ΔE = 0.1 V followed by stabilization of the current until the oxidation peak.

The observed peaks can be related to the redox reactions between Ni^{2+} and Ni^{3+} according to the reaction

$$Ni(OH)_2 + OH^- \rightleftarrows NiOOH + H_2O + e^-$$

This reaction is described in the literature[42,43] to involve the transport of protons and electrons into and out of the solid phase.

The difference in the maximum current observed at the redox peaks and the 7-fold increase in capacitance across the samples can be attributed to the nanostructuring of nickel. Ni-NR@NAA has a larger surface in contact with the electrolyte, giving rise to a larger number of active sites for the redox reaction to take place. Additionally, in the anodic part of the sweep for Ni-NR@NAA, the current is mainly devoted to the redox reactions, which in turn reduces the efficiency of the OER and shifts its onset to higher potentials.

The fast current increase and subsequent stabilization at the beginning of the anodic part of the CV curve are indicative of a capacitive component. This can also be attributed to the higher active surface in comparison with the pure Ni: a large amount of charge is necessary to build up the electrostatic double layer around the Ni nanopillars, giving rise to a measurable current at the beginning of the anodic sweep.

The study of the electrochemical properties of Ni-NR@NAA is presented in Figure 4. The data correspond to a sample with Q_{dep} = 2.5 C in the Ni deposition step (corresponding to a Ni mass loading of M = 410 μg).

Figure 4a shows the evolution of the CV as a function of the number of CV cycles, N, for five different N. Figure 4b plots the corresponding specific capacitances as a function of N. The CV curves show the two oxidation and reduction peaks as in Figure 4a, as well as the capacitive feature at the beginning of the anodic sweep. The oxidation peak appears at $E_{p,a}$ = 0.62 V for N = 1000 and remains essentially at $E_{p,a}$ = 0.59 V for N > 2000. On the other hand, the reduction peak starts at $E_{p,c}$ = 0.31 V and stabilizes at $E_{p,c}$ = 0.35 V for N > 3000. It is important to remark that the CV curves show a DC component (the curves are not symmetrical with respect to j = 0) with positive sign and that this DC component is reduced with the number of cycles.

The average current as a function of the cycle number is included in Figure S4. The evolution of the average current as a function of the cycle number can be modeled as the sum of two exponential decays, as shown in the Supporting Information. First, a fast decay is observed with a time constant of 6.3 × 10^3 s, followed by a slower decrease with a time constant of 2.1 × 10^5 s.

https://doi.org/10.1021/acsomega.5c01368
ACS Omega 2025, 10, 24618−24627

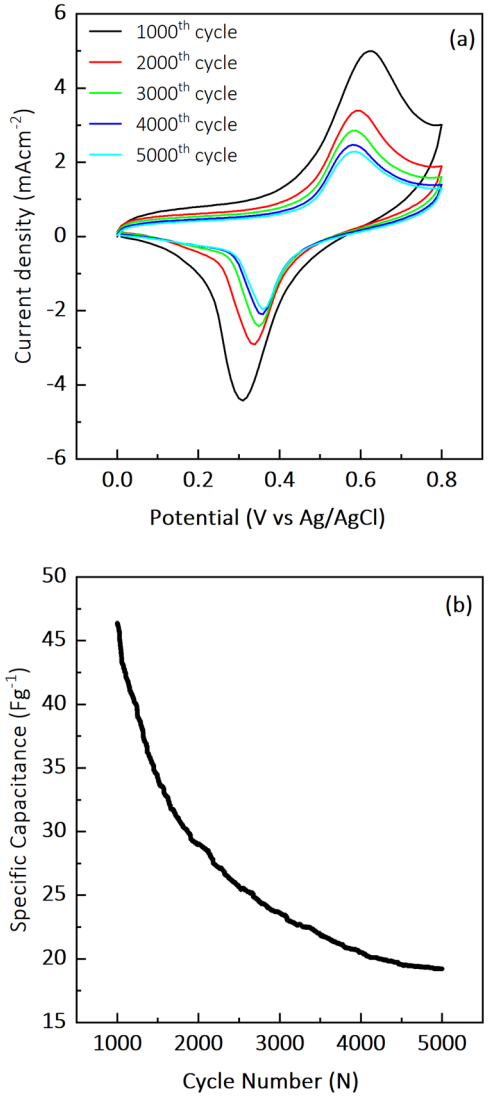

Figure 4. CV curve of Ni-NR@NAA as a working electrode with reference to Ag/AgCl in 1 M KOH solution (a) at different number of cycles and (b) its corresponding specific capacitance.

The observed positive DC component is related to the formation of $Ni(OH)_2$ from the oxidation of the deposited metallic nickel following the reaction

$$Ni + 2OH^- \rightleftarrows Ni(OH)_2 + 2e^-$$

In previous works,[44] this is described as the activation of the electrode, with a first oxidation of Ni to Ni^{2+} starting at a high rate and decaying exponentially as Ni-NR@NAA is covered by the hydroxide.

The effect of the electrode activation is also demonstrated by the evolution of the specific capacitance (Figure 4b). As the coverage and thickness of $Ni(OH)_2$ increases, the proton $[H^+]$ transport through the hydroxide layer becomes more difficult, thus lowering the current and the corresponding specific capacitance. The specific capacitance starts at C_s = 46.3 $F{\cdot}g^{-1}$ for N = 1000 and decreases until C_s = 19.2 $F{\cdot}g^{-1}$ for N = 5000, which corresponds to a capacitance retention of approximately 60% after 5000 cycles. As the behavior shown by the Ni-NR@NAA electrodes has a clear faradaic component, it is also common to express its performance in terms of charge. For the data shown in Figure 4b, we computed the specific charge following the procedure included in the Supporting Information. The resulting specific charge is also shown in Figure S6.

The study of the dependence of the electrochemical response of Ni-NR@NAA with the scan rate, ν, is presented in Figure 5, for a sample obtained with a deposition charge of Q_{dep} = 3 C (mass loading M = 501 μg). Figure 5a shows the measured CV curves at different scan rates obtained after the sample activation. Figure 5b shows the specific capacitance as a function of ν. Finally, Figure 5c shows the peak currents as a function of the square root of the scan rate.

It can be observed that the oxidation peaks reach higher values for bigger ν, while reduction peaks behave symmetrically, reaching lower values for bigger ν. The anodic peak current (oxidation) for ν = 5 mVs^{-1} is $i_{p,a}$ = 0.47 mA whereas for ν = 100 mVs^{-1} it increases up to $i_{p,a}$ = 3.59 mA. Likewise, the cathodic peak current (reduction) for ν = 5 mVs^{-1} is $i_{p,c}$ = −0.47 mA whereas for ν = 100 mVs^{-1}, it is $i_{p,c}$ = −3.74 mA.

The potential corresponding to the maximum current also shifts with increasing ν: to higher values for the oxidation peaks and to lower values for the reduction peaks. More concisely, the anodic peak for ν = 5 mVs^{-1} appears at a potential $E_{p,a}$ = 0.55 V, while for ν = 100 mVs^{-1} it appears at $E_{p,a}$ = 0.70 V. On the other hand, the cathodic peak appears at $E_{p,c}$ = 0.39 V for ν = 5 mVs^{-1} and at $E_{p,c}$ = 0.30 V for ν = 100 mVs^{-1}.

This observed behavior agrees with the abovementioned nickel hydroxide−nickel oxyhydroxide redox pair. The specific capacitance shows a decrease with an increasing scan rate. This is also described in the literature[42] as the transport of protons and electrons through the hydroxide−oxyhydroxide mixture is limited and cannot sustain the fast-varying potential at high rates.

Figure 5c shows the plot of both anodic and cathodic peak currents as a function of the square root of the scan rate. The linear dependences indicate the reversibility of the nickel hydroxide−nickel oxyhydroxide redox pair reactions.

Figure 6 corresponds to the electrochemical characterization of the redeposited electrodes (Ni-R-NR@NAA). In Figure 6a, the evolution of CV curves with the number of cycles is depicted. Figure 6b corresponds to the CV after sample activation for different scan rates. Finally, Figure 6c shows the specific capacitance as a function of the scan rate obtained from the CV curves in Figure 6b.

The CV curves shown in Figure 6a correspond to a Ni-R-NR@NAA sample obtained with a Q_{dep} = 3.5 C and a Q_{redep} = 1.5 C (correspond to the total Ni mass loading of 820 μg). The curves show mainly capacitive behavior with a fast change in current at the turning points from the cathodic to the anodic and from the anodic to the cathodic sweeps. The curves do not show any of the redox peaks observed for Ni-NR@NAA. The data indicate a clear DC component that decreases with an increasing number of cycles, N. This behavior is analogous to that observed for Ni-NR@NAA. The average current as a function of time is reported in Figure S5 and shows two different exponential decay regimes: a fast decay at the beginning with a time constant of $1.7{\cdot}10^3$ s, followed by a slower one with a time constant of $6.6{\cdot}10^5$ s.

The CV curves of Figure 6b depict the dependence of the CV curves on the scan rate. The measurements were obtained with a sample with Q_{dep} = 3.5 C and Q_{redep} = 1.5 C. All of the curves show the clear fast change in current at the start of the anodic and cathodic sweeps. For instance, at the start of the anodic sweep for ν = 5 mVs^{-1}, the current increases from j = $-6.9{\cdot}10^{-3}$ to j = $-1.3{\cdot}10^{-3}$ mA/cm^2 in the first 3.9 mV, while

https://doi.org/10.1021/acsomega.5c01368
ACS Omega 2025, 10, 24618−24627

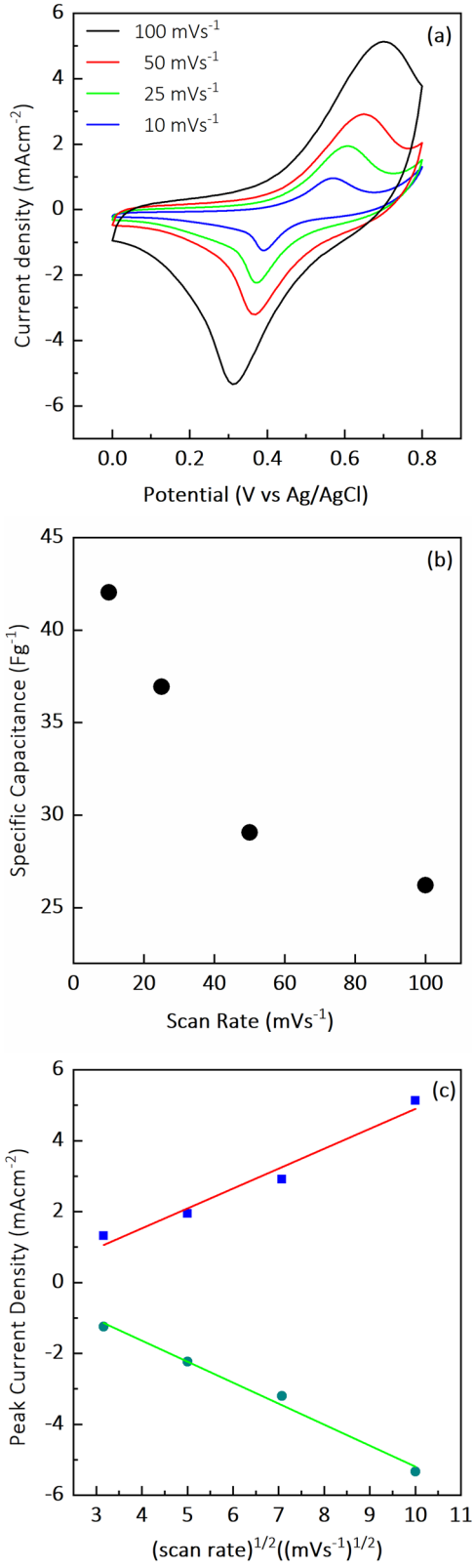

Figure 5. CV curve of Ni-NR@NAA nanorods as the working electrode with reference to Ag/AgCl in 1 M KOH solution (a) at different scan rates ranging from 10 to 100 mVs^{-1}, (b) its corresponding specific capacitance, and (c) plot of the peak current densities versus square root of scan rate for the anodic (red line) and cathodic (green line) sweeps of the CV.

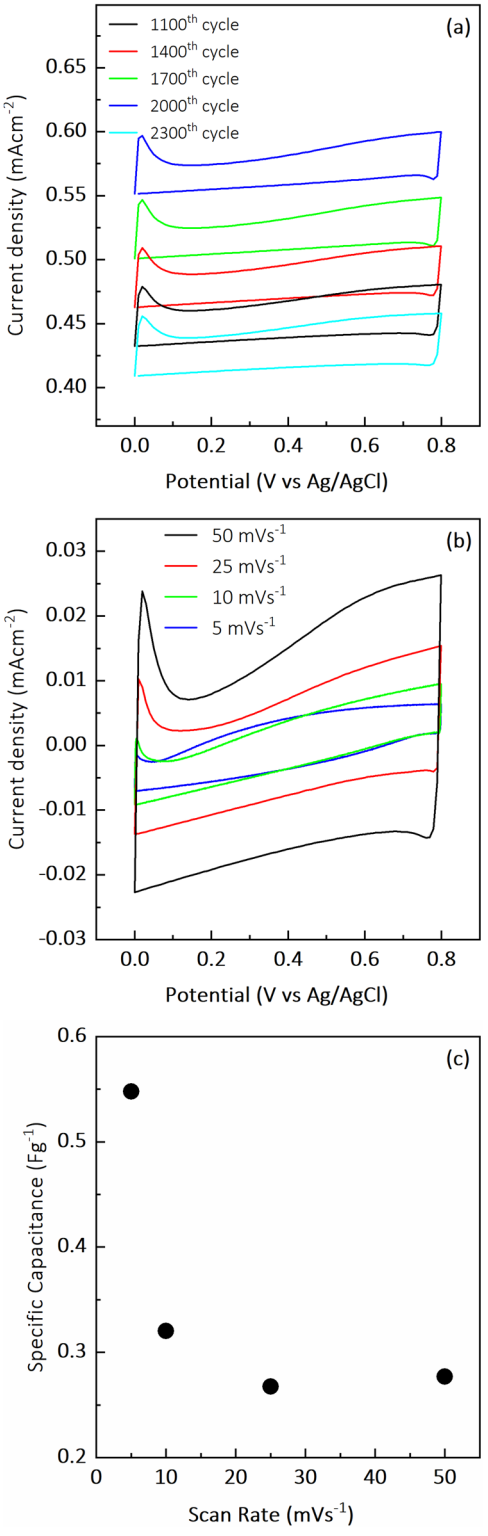

Figure 6. CV curve of Ni-R-NR@NAA nanorods as the working electrode with reference to Ag/AgCl in 1 M KOH solution (a) at different number of cycles, (b) at different scan rates ranging from 5 to 50 mVs^{-1}, and (c) corresponding specific capacitance at different scan rates.

for $\nu = 50$ mVs^{-1}, the increase is from $j = -2.3 \cdot 10^{-2}$ to $j = 2.4 \cdot 10^{-2}$ mA/cm^2 in the first 20 mV. After this fast start, the current decreases slowly until a local minimum is reached. For the mentioned curves, these local minima appear at $E = 43$ mV,

https://doi.org/10.1021/acsomega.5c01368
ACS Omega 2025, 10, 24618−24627

with a current density of $j = -2.6{\cdot}10^{-3}$ mA/cm^2 for $\nu = 5$ mVs^{-1}, while for $\nu = 50$ mVs^{-1}, the local minimum appears at $E = 140$ mV, with a current density of $j = 7.8{\cdot}10^{-3}$ mA/cm^2. This local minimum is then followed by a gradual increase for the rest of the anodic sweep. The maximum currents achieved are $i = 6.4{\cdot}10^{-3}$ mA/cm^2 for $\nu = 5$ mVs^{-1} and $i = 2.6{\cdot}10^{-2}$ mA/cm^2 for $\nu = 50$ mVs^{-1}.

Finally, Figure 6c shows the specific capacitances evaluated from the CV curves in Figure 6b. The specific capacitance as a function of the scan rate shows the same trend as with Ni-NR@NAA with a higher value at lower scan rates and a stabilization as the scan rate increases.

By comparing the behavior of the DC components between Ni-NR@NAA and Ni-R-NR@NAA, it can be concluded that in both cases the activation of the Ni electrode follows the same trend with two different regimes: a faster one at the beginning followed by a slower one. The main difference is that the time constant for the first regime is much lower for Ni-R-NR@NAA than for Ni-NR@NAA. This can be taken as an indication that the additional redeposited Ni has a faster reaction rate for the activation reaction. This faster activation together with the fact that the Ni mass is bigger can lead to a thicker Ni hydroxide layer in the case of Ni-R-NR@NAA, which makes proton transfer much more difficult and completely prevents redox reactions between Ni hydroxide and oxyhydroxide. This explains the only capacitive behavior of Ni-R-NR@NAA and the 2 orders of magnitude lower specific capacitance with respect to Ni-NR@NAA.

CONCLUSIONS

In this work, we studied the electrochemical properties of nickel nanorod structured electrodes obtained by pulsed electrodeposition onto aluminum substrates using nanoporous anodic alumina (NAA) as a template. The technique has been developed from previous works and permits one to obtain arrays of nickel nanorods within the pores of the NAA that maintain the electrical contact with the aluminum substrate. Samples prepared following two routes were obtained: nickel nanorods embedded in the partially dissolved NAA matrix (Ni-NR@NAA) and free-standing nickel nanorods with an additional conformal (re)deposited nickel layer (Ni-R-NR@NAA).

The results show that the nickel nanorods within the partially dissolved NAA electrodes (Ni-NR@NAA) demonstrate remarkable pseudocapacitive behavior with both redox activity and an electrochemical double layer capacitive component. The CV measurements show a 7-fold increase in capacitance per unit area with respect to flat nickel electrodes in CV experiments due to enhanced ion diffusion paths to the metal surface as well as a significantly higher active surface area. In addition, the use of nanostructured nickel nanorods shifts the onset of the oxygen evolution reaction (OER) to higher voltages compared with flat nickel. On the other hand, free-standing nickel nanorods with a redeposited nickel layer (Ni-R-NR@NAA) exhibited mainly a supercapacitive behavior with reduced redox activity.

Cyclic voltammetry (CV) studies in the KOH electrolyte show that the specific capacitance of Ni-NR@NAA evolves with the number of cycles applied during the experiment, tending to a stable value. Furthermore, a DC component in the CV curves is observed that decreases exponentially with the number of cycles. These indicate that the first cycles in the CV experiments produce the activation of the nickel by oxidizing the atoms closer to the interface to nickel hydroxide. After activation, the CV curves show a clear faradaic reversible behavior that can be explained by redox reactions of the nickel hydroxide−oxyhydroxide pair. The curves also show a small capacitive component at the beginning of the anodic sweep that indicates the formation of an electrochemical double layer before the oxidation reactions begin to take place. The results reveal that the Ni-NR@NAA electrodes can reach specific capacitances up to 60 F·g^{-1} at a scan rate of 5 mVs^{-1}, and this specific capacitance decreases with increasing scan rate.

Finally, the full removal of the NAA and the redeposition of a thin layer of nickel onto the aluminum substrate and on the nanorods array (Ni-R-NR@NAA) result in an almost complete suppression of the redox activity on the sample surface. This indicates that the nickel deposited after oxide removal produces a nickel hydroxide with substantially different ion conduction properties that prevent the redox reactions at the hydroxide−metal interface. This results in a much-reduced specific capacitance for the case of Ni-R-NR@AAO, reaching upto 0.8 F·g^{-1} at 5 mVs^{-1} scan rate.

The comparison between these two electrode designs reveals the influence of structural modifications on electrochemical properties, particularly in terms of ion transport and redox reaction efficiency. These findings highlight the importance of controlled nanostructuring in achieving an optimized performance for energy storage systems. The knowledge about the developed self-supported nickel electrodes not only provides details into tailored electrochemical behavior but also opens new possibilities for advanced supercapacitor or pseudocapacitor applications.

ASSOCIATED CONTENT

Supporting Information

The Supporting Information is available free of charge at https://pubs.acs.org/doi/10.1021/acsomega.5c01368.

PVC casing with aluminum samples mounted on a copper plate base (anode), SEM images of NAA showing top and cross-sectional views (a) before and (b) after barrier layer removal, SEM images of Ni@NAA after pulsed electrodeposition including cross-sectional and top views, DC current decay over time for electrodes exhibiting pseudocapacitive and supercapacitive behaviors in CV tests, calculations of capacitance and specific capacitance from CV measurements, and the plot of specific charge as a function of cycle number for Ni-NR@NAA sample (PDF)

AUTHOR INFORMATION

Corresponding Author

Josep Ferre-Borrull − *Universitat Rovira i Virgili, Departament d'Enginyeria Electrònica, Elèctrica i Automàtica, Tarragona 43007, Spain;* orcid.org/0000-0002-5210-5133; Email: josep.ferre@urv.cat

Authors

Tabish Aftab − *Universitat Rovira i Virgili, Departament d'Enginyeria Electrònica, Elèctrica i Automàtica, Tarragona 43007, Spain*

Lluis F. Marsal − *Universitat Rovira i Virgili, Departament d'Enginyeria Electrònica, Elèctrica i Automàtica, Tarragona 43007, Spain;* orcid.org/0000-0002-5976-1408

Complete contact information is available at:

https://pubs.acs.org/10.1021/acsomega.5c01368

Author Contributions

T.A.: Methodology, investigation, formal analysis, writing—review and editing, software, data curation; J.F.-B.: supervision, conceptualization, investigation, formal analysis; L.F.M.: methodology, funding acquisition, conceptualization, resources.

Notes

The authors declare no competing financial interest.

■ ACKNOWLEDGMENTS

The authors acknowledge the financial support through the predoctoral grant provided by the Agency for Management of University and Research Grants (AGAUR-FI Predoctoral Program, 2021 FI-00365) Joan Oró, under the Secretaria d'Universitats i Recerca of the Departament de Recerca i Universitats, Generalitat de Catalunya, and cofunded by the European Social Plus Funds. This project also received funding from the AGAUR-2021 SGR 00739 GRC Grant, as well as the Spanish Ministerio de Ciencia e Innovación (MICINN) under Project PDI2021-128342OB-I00. Additional support was provided by the Catalan Institution for Research and Advanced Studies (ICREA) through the ICREA Academia Award 2021. The authors further acknowledge the NETPORE COST Action CA20126 for its support.

■ REFERENCES

(1) Miller, J. R.; Simon, P. Electrochemical capacitors for energy management. *Science* **2008**, *321*, 651−652.
(2) Winter, M.; Brodd, R. J. What are batteries, fuel cells, and supercapacitors? *Chem. Rev.* **2004**, *104*, 4245−4270.
(3) Conway, B. E.*Electrochemical Supercapacitors: Scientific Fundamentals and Technological Applications*; Springer: New York, 2013.
(4) Dubal, D. P.; Ayyad, O.; Ruiz, V.; Gomez-Romero, P. Hybrid energy storage: the merging of battery and supercapacitor chemistries. *Chem. Soc. Rev.* **2015**, *44*, 1777−1790.
(5) Jiang, H.; Lee, P. S.; Li, C. 3D Carbon based nanostructures for advanced supercapacitors. *Energy Environ. Sci.* **2013**, *6*, 41−53.
(6) Zhang, L.; Wang, J.; Zhu, J.; Zhang, X.; San Hui, K.; Hui, K. N. 3D porous layered double hydroxides grown on graphene as advanced electrochemical pseudocapacitor materials. *J. Mater. Chem. A* **2013**, *1* (1), 9046−9053.
(7) Simon, P.; Gogotsi, Y. Materials for electrochemical capacitors. *Nat. Mater.* **2008**, *7*, 845−854.
(8) Wang, G.; Zhang, L.; Zhang, J. A review of electrode materials for electrochemical supercapacitors. *Chem. Soc. Rev.* **2012**, *41*, 797−828.
(9) Shi, Y.; Li, M.; Yu, Y.; Zhang, B. Recent advances in nanostructured transition metal phosphides: synthesis and energy-related applications. *Energy Environ. Sci.* **2020**, *13*, 4564−4582.
(10) Choi, H.; Yoon, H. Nanostructured electrode materials for electrochemical capacitor applications. *Nanomaterials* **2015**, *5*, 906−936.
(11) Yu, G.; Xie, X.; Pan, L.; Bao, Z.; Cui, Y. Hybrid nanostructured materials for high-performance electrochemical capacitors. *Nano Energy* **2013**, *2*, 213−234.
(12) Jiang, L. B.; Yuan, X. Z.; Liang, J.; Zhang, J.; Wang, H.; Zeng, G. M. Nanostructured core-shell electrode materials for electrochemical capacitors. *J. Power Sources* **2016**, *331*, 408−425.
(13) Vidhyadharan, B.; Zain, N. K.; Misnon, I. I.; Aziz, R. A.; Ismail, J.; Yusoff, M. M.; Jose, R. High performance supercapacitor electrodes from electrospun nickel oxide nanowires. *J. Alloys Compd.* **2014**, *610*, 143−150.
(14) Cheng, S.; Yang, L.; Liu, Y.; Lin, W.; Huang, L.; Chen, D.; Wong, C. P.; Liu, M. Carbon fiber paper supported hybrid nanonet/nanoflower nickel oxide electrodes for high-performance pseudocapacitors. *J. Mater. Chem. A* **2013**, *1* (1), 7709−7716.
(15) Sun, W.; Chen, L.; Meng, S.; Wang, Y.; Li, H.; Han, Y.; Wei, N. Synthesis of NiO nanospheres with ultrasonic method for supercapacitors. *Mater. Sci. Semicond. Process.* **2014**, *17*, 129−133.
(16) Inamdar, A. I.; Kim, Y.; Pawar, S. M.; Kim, J. H.; Im, H.; Kim, H. Chemically grown, porous, nickel oxide thin-film for electrochemical supercapacitors. *J. Power Sources* **2011**, *196*, 2393−2397.
(17) Xu, W.; Zhao, X.; Zhan, F.; He, Q.; Wang, H.; Chen, J.; Wang, H.; Ren, X.; Chen, L. Toward emerging two-dimensional nickel-based materials for electrochemical energy storage: Progress and perspectives. *Energy Storage Mater.* **2022**, *53*, 79−135.
(18) Verma, S.; Arya, S.; Gupta, V.; Mahajan, S.; Furukawa, H.; Khosla, A. Performance analysis, challenges and future perspectives of nickel based nanostructured electrodes for electrochemical supercapacitors. *J. Mater. Res. Technol.* **2021**, *11*, 564−599.
(19) Wang, Y.; Song, Y.; Xia, Y. Electrochemical capacitors: mechanism, materials, systems, characterization and applications. *Chem. Soc. Rev.* **2016**, *45*, 5925−5950.
(20) Huang, J.; Xie, Y.; You, Y.; Yuan, J.; Xu, Q.; Xie, H.; Chen, Y. Rational design of electrode materials for advanced supercapacitors: from lab research to commercialization. *Adv. Funct. Mater.* **2023**, *33*, No. 2213095.
(21) Lee, W. Structural Engineering of Porous Anodic Aluminum Oxide (AAO) and Applications. In *Nanoporous Alumina: Fabrication, Structure, Properties and Applications*; Losic, D.; Santos, A., Eds.; Springer: Cham, 2015; pp 107−153.
(22) Masuda, H.; Fukuda, K. Ordered metal nanohole arrays made by a two-step replication of honeycomb structures of anodic alumina. *Science* **1995**, *268*, 1466−1468.
(23) Ferré-Borrull, J.; Pallarès, J.; Macías, G.; Marsal, L. F. Nanostructural engineering of nanoporous anodic alumina for biosensing applications. *Materials* **2014**, *7*, 5225−5253.
(24) Balderrama, V. S.; Albero, J.; Granero, P.; Ferré-Borrull, J.; Pallarès, J.; Palomares, E.; Marsal, L. F. Design, fabrication and charge recombination analysis of an interdigitated heterojunction nanomorphology in P3HT/PC 70 BM solar cells. *Nanoscale* **2015**, *7*, 13848−13859.
(25) Palacios, R.; Formentin, P.; Martinez-Ferrero, E.; Pallarès, J.; Marsal, L. F. β-Phase morphology in ordered poly (9, 9-dioctylfluorene) nanopillars by template wetting method. *Nanoscale Res. Lett.* **2011**, *6*, No. 35.
(26) Santos, A.; Vojkuvka, L.; Pallarès, J.; Ferré-Borrull, J.; Marsal, L. F. Cobalt and nickel nanopillars on aluminium substrates by direct current electrodeposition process. *Nanoscale Res. Lett.* **2009**, *4*, 1021−1028.
(27) Eessaa, A. K.; El-Shamy, A. M. Review on fabrication, characterization, and applications of porous anodic aluminum oxide films with tunable pore sizes for emerging technologies. *Microelectron. Eng.* **2023**, *279*, No. 112061.
(28) Liu, C. Y.; Wang, Y. L. Creating anodic alumina nanochannel arrays with custom-made geometry. *J. Chin. Chem. Soc.* **2020**, *67*, 11−24.
(29) Domagalski, J. T.; Xifre-Perez, E.; Marsal, L. F. Recent advances in nanoporous anodic alumina: Principles, engineering, and applications. *Nanomaterials* **2021**, *11*, No. 430.
(30) Nie, M.; Sun, H.; Gao, Z. D.; Li, Q.; Xue, Z. H.; Luo, J.; Liao, J. M. Co−Ni nanowires supported on porous alumina as an electrocatalyst for the hydrogen evolution reaction. *Electrochem. Commun.* **2020**, *115*, No. 106719.
(31) Han, F.; Meng, G.; Zhou, F.; Song, L.; Li, X.; Hu, X.; Zhu, X.; Wu, B.; Wei, B. Dielectric capacitors with three-dimensional nanoscale interdigital electrodes for energy storage. *Sci. Adv.* **2015**, *1*, No. e1500605.
(32) Xu, J.; Gao, L.; Cao, J.; Wang, W.; Chen, Z. Preparation and electrochemical capacitance of cobalt oxide (Co3O4) nanotubes as supercapacitor material. *Electrochim. Acta* **2010**, *56*, 732−736.
(33) Xu, J.; Gao, L.; Cao, J.; Wang, W.; Chen, Z. Electrochemical capacitance of nickel oxide nanotubes synthesized in anodic

aluminum oxide templates. *J. Solid State Electrochem.* **2011**, *15*, 2005−2011.
(34) Nakanishi, H.; Kikuta, I.; Kawabata, Y.; Norisuye, T.; Tran-Cong-Miyata, Q.; Segawa, H. Fast Ion and Electron Transport in a Supercapacitor Based on Monolithic Nanowire-Array Electrodes Prepared from a Defect-Free Anodic Aluminium Oxide Mold. *Adv. Mater. Interfaces* **2015**, *2*, No. 1500354.
(35) González, A. S.; Fernández, J. G.; Martínez, V. V.; Flores, R. C.; Pidal, V. M. P. High-Performance 3D Nanostructured Silver Electrode for Micro-Supercapacitor Application. *ACS Omega* **2023**, *8*, 40087−40098.
(36) Santos, A.; Formentín, P.; Pallarès, J.; Ferré-Borrull, J.; Marsal, L. F. Structural engineering of nanoporous anodic alumina funnels with high aspect ratio. *J. Electroanal. Chem.* **2011**, *655*, 73−78.
(37) Santos, A.; Ferré-Borrull, J.; Pallarès, J.; Marsal, L. F. Hierarchical nanoporous anodic alumina templates by asymmetric two-step anodization. *Phys. Status Solidi A* **2011**, *208*, 668−674.
(38) Santos, A.; Vojkuvka, L.; Alba, M.; Balderrama, V. S.; Ferré-Borrull, J.; Pallarès, J.; Marsal, L. F. Understanding and morphology control of pore modulations in nanoporous anodic alumina by discontinuous anodization. *Phys. Status Solidi A* **2012**, *209*, 2045−2048.
(39) Santos, A.; Vojkuvka, L.; Pallarés, J.; Ferré-Borrull, J.; Marsal, L. F. In situ electrochemical dissolution of the oxide barrier layer of porous anodic alumina fabricated by hard anodization. *J. Electroanal. Chem.* **2009**, *632*, 139−142.
(40) Nielsch, K.; Müller, F.; Li, A. P.; Gösele, U. Uniform nickel deposition into ordered alumina pores by pulsed electrodeposition. *Adv. Mater.* **2000**, *12*, 582−586.
(41) Aftab, T.; Almora, O.; Ferre-Borrull, J.; Marsal, L. F. 3D Nanostructured Electrodes Based on Anodic Alumina Templates for Stable Pseudocapacitors. *Phys. Status Solidi RRL* **2024**, *18*, No. 2400144.
(42) Patil, U. M.; Gurav, K. V.; Fulari, V. J.; Lokhande, C. D.; Joo, O. S. Characterization of honeycomb-like "β-Ni (OH) 2" thin films synthesized by chemical bath deposition method and their supercapacitor application. *J. Power Sources* **2009**, *188*, 338−342.
(43) Tang, Z.; Tang, C. H.; Gong, H. A high energy density asymmetric supercapacitor from nano-architectured Ni (OH) 2/Carbon nanotube electrodes. *Adv. Funct. Mater.* **2012**, *22*, 1272−1278.
(44) Liu, L.; Zhao, Y.; Zhou, Q.; Xu, H.; Zhao, C.; Jiang, Z. Nano-polypyrrole supercapacitor arrays prepared by layer-by-layer assembling method in anodic aluminum oxide templates. *J. Solid State Electrochem.* **2007**, *11*, 32−37.

https://doi.org/10.1021/acsomega.5c01368
ACS Omega 2025, 10, 24618−24627